Phase transitions and domain structures in strained pseudocubic (100) SrTiO$_3$ thin films

Y. L. Li,[1,2,*] S. Choudhury,[1] J. H. Haeni,[1] M. D. Biegalski,[1] A. Vasudevarao,[1] A. Sharan,[1] H. Z. Ma,[3] J. Levy,[3]
Venkatraman Gopalan,[1] S. Trolier-McKinstry,[1] D. G. Schlom,[1] Q. X. Jia,[2] and L. Q. Chen[1]

[1]*Department of Materials Science and Engineering, The Pennsylvania State University, University Park, Pennsylvania 16802, USA*
[2]*MST-STC, MS K763, Los Alamos National Lab, Los Alamos, New Mexico 87545, USA*
[3]*Department of Physics and Astronomy, University of Pittsburgh, Pittsburgh, Pennsylvania 15260, USA*

The mutual interactions between a structural transition and a ferroelectric transition are analyzed for different strain states in a pseudocubic (100) SrTiO$_3$ film by examining the equilibrium solutions of the total free energy as a function of polarization, strain and structural order parameter. The range of possible ferroelectric transition temperatures and the possible ferroelectric states of a strained SrTiO$_3$ film are determined with respect to the variation in the reported properties of bulk SrTiO$_3$ single crystals. The ferroelectric and structural domain morphologies at a biaxial tensile strain $e_0=0.94\%$ were predicted using phase-field simulations. It is shown that variations in the reported values of bulk properties and in the Landau energy coefficients from different literature sources lead not only to a wide range of possible transition temperatures at a given strain, but also to different ferroelectric states (e.g., polarization along the pseudocubic $\langle 110 \rangle$ vs $\langle 100 \rangle$ directions) thus different domain structures under a biaxial tensile strain. Both optical second harmonic generation and confocal scanning optical microscopy measurements demonstrate that the domain states in SrTiO$_3$ films strained at $e_0=0.94\%$ and 1.16% exhibit polar directions along the pseudocubic $\langle 110 \rangle$ directions within the pseudocubic (001) plane of the film.

I. INTRODUCTION

Strontium titanate (SrTiO$_3$) is known as an incipient ferroelectric or quantum paraelectric since pure SrTiO$_3$ remains paraelectric down to 0 K under stress-free conditions, but has a ferroelectric instability manifested by large dielectric constants at low temperature.[1,2] It is well established that SrTiO$_3$ undergoes an antiferrodistortive (AFD) phase transition from cubic to tetragonal symmetry at ~105 K, which is associated with rotations of the TiO$_6$ octahedra about one of the cubic axes.[3,4] It has been suggested that the ferroelectric transition might be suppressed by this preceding AFD phase transition,[5–7] in addition to the quantum fluctuations of the atoms about their centrosymmetric positions,[2,8] i.e., the tetragonal distortions prevent the ferroelectric transition. It was proposed that SrTiO$_3$ would have a ferroelectric transition around 30 K if there was no intervening structural transition.[6]

Due to its high dielectric constants and low microwave losses at cryogenic temperatures, SrTiO$_3$ is an ideal candidate for electrically tunable microwave devices. For many applications, thin film structures are required since they can reduce the operating voltages and are compact. The desire to maximize dielectric tunability while minimizing dispersion at microwave frequencies requires that candidate films operate at temperatures slightly above the ferroelectric transition temperature T_c. In order to increase T_c, and thus the operating temperature, chemical substitution has been employed. For example, the T_c of Ba$_x$Sr$_{1-x}$TiO$_3$, a material widely investigated for these applications, can be chemically tuned from close to 0 K for nearly pure SrTiO$_3$ to 403 K for pure BaTiO$_3$.[9] Local structural and compositional inhomogeneities can, however, produce nonuniform strains. Nonuniform strains may be responsible for polarization variations that could suppress ferroelectricity due to internal depoling fields[10,11] and the significant inhomogeneous broadening of the peak in ε_r vs temperature (T) observed in the vast majority of ferroelectric thin films,[12,13] which is detrimental to many applications. An alternative method to enhance T_c is to uniformly strain a film by utilizing the lattice mismatch between an epitaxial film and the underlying substrate. Indeed, it was recently discovered that a strained epitaxial SrTiO$_3$ thin film grown on a dysprosium scandate (DyScO$_3$) substrate is ferroelectric near room temperature, resulting from a nearly 0.94% tensile in-plane strain.[14,15]

Strain-induced enhancement of T_c has been predicted previously in SrTiO$_3$ using thermodynamics[16] although the predicted T_c (~204 K) is significantly lower than that determined experimentally.[14] An extensive literature search of the properties of bulk SrTiO$_3$ single crystals reveals significant variations among measurements made by different groups, and thus significantly different values for coefficients in a Landau description for both the structural and ferroelectric phase transitions. Therefore, one of the purposes of this paper is to examine the effect that differences among the measured values of relevant physical properties have on the predicted ferroelectric transition temperatures, as well as on the ferroelectric states of biaxially strained SrTiO$_3$ thin films. It will be shown below that the variation in the materials constants can lead to a wide range of possible ferroelectric transition temperatures and even different ferroelectric states with different directions of electric polarization. We will also describe the interactions between the AFD structural transition and the ferroelectric transition at different strains. Finally, we predict the possible domain structures as a result of both structural and ferroelectric transitions, as well as their

interactions when a pseudocubic (100) $SrTiO_3$ film is subject to $\sim 0.94\%$ tensile biaxial strain, corresponding to the case of a 500-Å-thick pseudocubic (100)-oriented $SrTiO_3$ film on a (110)-oriented $DyScO_3$ substrate.[14,15] It will be demonstrated that the variation in the Landau coefficients (due to differences among measured property values) leads to two possible ferroelectric states, and thus two types of possible domain structures under tensile biaxial strains. Therefore, we performed both optical second harmonic generation (SHG) and electro-optic confocal scanning optical microscopy (CSOM) measurements on pseudocubic (100) $SrTiO_3$ films grown on (110) $DyScO_3$ substrates. Analyses of both the SHG signals and CSOM electro-optic responses showed that the ferroelectric state is orthorhombic with the polarization along the pseudocubic $\langle 110 \rangle$ directions within the plane of the pseudocubic (001) $SrTiO_3$ film.

II. THERMODYNAMIC DESCRIPTION

To describe a proper ferroelectric transition and an AFD structural transition, the spontaneous polarization **p** $=(p_1, p_2, p_3)$ and the structural order parameter $\mathbf{q}=(q_1, q_2, q_3)$ are chosen as the order parameters. The structural order parameter represents the linear oxygen displacement that corresponds to simultaneous out-of-phase rotations of oxygen octahedra around one of their fourfold symmetry axes.[17] Polarization measurements show that the ferroelectric transition in $SrTiO_3$ thin films is of second order,[18] and hence a fourth-order polynomial in the components of the polarization and of the oxygen displacement is employed[16,19,20] in the stress-free Landau free energy expansion, i.e.,

$$f_{bulk}(p_i, q_i) = A_{ij}p_ip_j + A_{ijkl}p_ip_jp_kp_l + B_{ij}q_iq_j + B_{ijkl}q_iq_jq_kq_l$$
$$+ C_{ijkl}p_ip_jq_kq_l, \tag{1}$$

where i, $j=1,2,3$; A_{ijkl}, B_{ijkl}, and C_{ijkl} are constant, and A_{ij} and B_{ij} are functions of temperature. It should be emphasized that all the coefficients in Eq. (1) are measured under stress-free conditions. In this paper, we follow the usual Einstein summation convention, i.e., the repeated indices in a given term imply summation over them. In Eq. (1), only the terms allowed by the cubic symmetry of the $SrTiO_3$ crystal are nonzero, i.e.

$$f_{bulk} = \alpha_1(p_1^2 + p_2^2 + p_3^2) + \alpha_{11}(p_1^4 + p_2^4 + p_3^4) + \alpha_{12}(p_1^2p_2^2 + p_2^2p_3^2 + p_3^2p_1^2) + \beta_1(q_1^2 + q_2^2 + q_3^2) + \beta_{11}(q_1^4 + q_2^4 + q_3^4)$$
$$+ \beta_{12}(q_1^2q_2^2 + q_2^2q_3^2 + q_3^2q_1^2) - t_{11}(p_1^2q_1^2 + p_2^2q_2^2 + p_3^2q_3^2)$$
$$- t_{12}[p_1^2(q_2^2 + q_3^2) + p_2^2(q_1^2 + q_3^2) + p_3^2(q_1^2 + q_2^2)]$$
$$- t_{44}(p_1p_2q_1q_2 + p_2p_3q_2q_3 + p_3p_1q_3q_1), \tag{2}$$

where α_{ij}, β_{ij}, and t_{ij} are assumed to be constants and α_1 and β_1 depend on temperature.

If a single crystal is strained, there is an elastic energy contribution to the total free energy. Using linear elasticity, the elastic energy density is

$$f_{elastic}(p_i, q_i, \varepsilon_{ij}) = \tfrac{1}{2}c_{ijkl}e_{ij}e_{kl} = \tfrac{1}{2}c_{ijkl}(\varepsilon_{ij} - \varepsilon_{ij}^0)(\varepsilon_{kl} - \varepsilon_{kl}^0), \tag{3}$$

where c_{ijkl} is the elastic stiffness tensor, $e_{ij} = \varepsilon_{ij} - \varepsilon_{ij}^0$ is elastic strain, ε_{ij} is the strain state compared to the parent cubic paraelectric phase, and ε_{ij}^0 is the stress-free strain or the transformation strain as a result of the structural and/or ferroelectric transitions

$$\varepsilon_{ij}^0 = Q_{ijkl}p_kp_l + \Lambda_{ijkl}q_kq_l, \tag{4}$$

in which Q_{ijkl} and Λ_{ijkl} represent, respectively, the electrostrictive coefficient and the linear-quadratic coupling coefficient between the strain and the structural order parameter.

Now consider a $(100)_p$-oriented $SrTiO_3$ thin film with a stress-free surface that is subject to a biaxial substrate constraint, where the subscript p refers to the pseudocubic Miller index. A rectangular coordinate system, $\mathbf{x} = (x_1, x_2, x_3)$, is set up with the x_1, x_2, and x_3 axes along the $[100]_p$, $[010]_p$, and $[001]_p$ crystallographic directions of the cubic $SrTiO_3$ film. The macro substrate constraint is then described by the average biaxial strain e_0, i.e., $\bar\varepsilon_{11} = \bar\varepsilon_{22} = e_0$, $\bar\varepsilon_{12} = 0$. Although the average biaxial strains need not be equal along the two in-plane directions of the film [and for $SrTiO_3$ grown on (110) $DyScO_3$, $\bar\varepsilon_{11}$ differs slightly from $\bar\varepsilon_{22}$], in this paper we limit our analysis to the case where $\bar\varepsilon_{11} = \bar\varepsilon_{22}$. If a single-domain state is assumed, i.e., the polarization and the structural order parameter are uniform throughout the entire film, the stress and strain fields are homogeneous in the film as well. Therefore

$$\varepsilon_{11} = \varepsilon_{22} = e_0, \quad \varepsilon_{12} = 0. \tag{5}$$

To satisfy the stress-free surface boundary condition, the other three strain components must satisfy

$$\sigma_{i3} = \partial f_{elastic}/\partial e_{i3} = 0, \tag{6}$$

where $i=1$, 2, and 3. Solving Eq. (6) by considering cubic symmetry, we have

$$\varepsilon_{13} = Q_{44}p_1p_3 + \Lambda_{44}q_1q_3, \quad \varepsilon_{23} = Q_{44}p_2p_3 + \Lambda_{44}q_2q_3,$$

$$\varepsilon_{33} = \lfloor g_{12}(p_1^2 + p_2^2) + g_{11}p_3^2 + \lambda_{12}(q_1^2 + q_2^2) + \lambda_{11}q_3^2$$
$$- 2c_{12}e_0\rfloor/c_{11}, \tag{7}$$

where $g_{11} = c_{11}Q_{11} + 2c_{12}Q_{12}$, $g_{12} = c_{11}Q_{12} + c_{12}(Q_{11} + Q_{12})$, $\lambda_{11} = c_{11}\Lambda_{11} + 2c_{12}\Lambda_{12}$, $\lambda_{12} = c_{11}\Lambda_{12} + c_{12}(\Lambda_{11} + \Lambda_{12})$, and the c_{ij}, Q_{ij}, and Λ_{ij} tensor components are in Voigt's notations of c_{ijkl}, Q_{ijkl}, and Λ_{ijkl}, respectively. Substituting all the strain components in Eqs. (5) and (7) into the elastic energy expression in Eq. (3), we have the equilibrium elastic strain energy of the pseudocubic film under a biaxial strain, e_0

$$f_{elastic}^f = \Delta\alpha_1^f(p_1^2 + p_2^2) + \Delta\alpha_3^f p_3^2 + \Delta\alpha_{11}^f(p_1^4 + p_2^4) + \Delta\alpha_{33}^f p_3^4$$
$$+ \Delta\alpha_{12}^f p_1^2 p_2^2 + \Delta\alpha_{13}^f(p_2^2 p_3^2 + p_1^2 p_3^2) + \Delta\beta_1^f(q_1^2 + q_2^2)$$
$$+ \Delta\beta_3^f q_3^2 + \Delta\beta_{11}^f(q_1^4 + q_2^4) + \Delta\beta_{33}^f q_3^4 + \Delta\beta_{12}^f q_1^2 q_2^2$$
$$+ \Delta\beta_{13}^f(q_2^2 q_3^2 + q_1^2 q_3^2) - \Delta t_{11}^f(p_1^2 q_1^2 + p_2^2 q_2^2) - \Delta t_{33}^f p_3^2 q_3^2$$
$$- \Delta t_{12}^f(p_1^2 q_2^2 + p_2^2 q_1^2) - \Delta t_{13}^f(p_1^2 + p_2^2)q_3^2 - \Delta t_{31}^f p_3^2(q_1^2$$
$$+ q_2^2) - \Delta t_{44}^f p_1 p_2 q_1 q_2 + \frac{1}{c_{11}}(c_{11}^2 + c_{11}c_{12} - 2c_{12}^2)e_0^2, \tag{8}$$

where the superscript f indicates the film, Δ means the changes of the corresponding coefficients in Eq. (2) due to the elastic interaction, and

$$\Delta\alpha_1^f = -\frac{(c_{11}-c_{12})(c_{11}+2c_{12})(Q_{11}+Q_{12})}{c_{11}}e_0, \quad \Delta\alpha_3^f = -\frac{2(c_{11}-c_{12})(c_{11}+2c_{12})Q_{12}}{c_{11}}e_0,$$

$$\Delta\alpha_{11}^f = \frac{(c_{11}-c_{12})(c_{12}(Q_{11}+Q_{12})^2 + c_{11}(Q_{11}^2+Q_{12}^2)}{2c_{11}}, \quad \Delta\alpha_{33}^f = \frac{(c_{11}-c_{12})(c_{11}+2c_{12})Q_{12}^2}{c_{11}},$$

$$\Delta\alpha_{12}^f = \frac{2c_{11}^2 Q_{11}Q_{12} - c_{12}^2(Q_{11}+Q_{12})^2 + c_{11}c_{12}(Q_{11}^2+Q_{12}^2) + 2c_{11}c_{44}Q_{44}^2}{c_{11}},$$

$$\Delta\alpha_{13}^f = \frac{(c_{11}-c_{12})(c_{11}+2c_{12})Q_{12}(Q_{11}+Q_{12})}{c_{11}},$$

$$\Delta\beta_1^f = -\frac{(c_{11}-c_{12})(c_{11}+2c_{12})(\Lambda_{11}+\Lambda_{12})}{c_{11}}e_0, \quad \Delta\beta_3^f = -\frac{2(c_{11}-c_{12})(c_{11}+2c_{12})\Lambda_{12}}{c_{11}}e_0,$$

$$\Delta\beta_{11}^f = \frac{(c_{11}-c_{12})(c_{12}(\Lambda_{11}+\Lambda_{12})^2 + c_{11}(\Lambda_{11}^2+\Lambda_{12}^2)}{2c_{11}}, \quad \Delta\beta_{33}^f = \frac{(c_{11}-c_{12})(c_{11}+2c_{12})\Lambda_{12}^2}{c_{11}},$$

$$\Delta\beta_{12}^f = \frac{2c_{11}^2 \Lambda_{11}\Lambda_{12} - c_{12}^2(\Lambda_{11}+\Lambda_{12})^2 + c_{11}c_{12}(\Lambda_{11}^2+\Lambda_{12}^2) + 2c_{11}c_{44}\Lambda_{44}^2}{c_{11}},$$

$$\Delta\beta_{13}^f = \frac{(c_{11}-c_{12})(c_{11}+2c_{12})\Lambda_{12}(\Lambda_{11}+\Lambda_{12})}{c_{11}},$$

$$\Delta t_{11}^f = -\frac{(c_{11}-c_{12})[c_{12}(Q_{11}+Q_{12})(\Lambda_{11}+\Lambda_{12}) + c_{11}(Q_{11}\Lambda_{11}+Q_{12}\Lambda_{12})]}{c_{11}},$$

$$\Delta t_{33}^f = -\frac{2(c_{11}-c_{12})(c_{11}+2c_{12})Q_{12}\Lambda_{12}}{c_{11}},$$

$$\Delta t_{12}^f = -\frac{(c_{11}-c_{12})[c_{12}(Q_{11}+Q_{12})(\Lambda_{11}+\Lambda_{12}) + c_{11}(Q_{12}\Lambda_{11}+Q_{11}\Lambda_{12})]}{c_{11}},$$

$$\Delta t_{13}^f = -\frac{(c_{11}-c_{12})(c_{11}+2c_{12})(Q_{11}+Q_{12})\Lambda_{12}}{c_{11}}, \quad \Delta t_{31}^f = -\frac{(c_{11}-c_{12})(c_{11}+2c_{12})(\Lambda_{11}+\Lambda_{12})Q_{12}}{c_{11}},$$

$$\Delta t_{44}^f = -4c_{44}Q_{44}\Lambda_{44}.$$

The sum of the bulk Landau free energy and the film elastic energy, $f = f_{bulk} + f_{elastic}^f$ gives the total free energy of a $(100)_p$-oriented SrTiO$_3$ film subject to a uniform biaxial constraint, e_0. This free energy will be employed below to analyze the phase transitions and their interactions. It should be noted that the free energy is obtained under the assumptions: (1) the film consists of a single domain, i.e., the domain wall energy is not included, (2) the thickness of the film is much

smaller than its underlying substrate so the constraint on the film from the substrate can be described by the biaxial strain e_0, and (3) a short-circuit electric surface boundary condition is employed so that the dipole-dipole interaction and the depolarization effect are ignored. It is easy to see that the introduction of elastic energy modifies the coefficients of both the quadratic and fourth-order terms of the polarization and the AFD structural order parameter in the bulk free energy

polynomial in Eq. (2). Therefore, the biaxial strain will affect the transition temperatures of both the ferroelectric phase and the AFD structural phase and their interactions.

III. RESULTS AND DISCUSSIONS

A. Range of ferroelectric transition temperature in SrTiO₃ films

From Eq. (8) it is seen that the elastic energy does not change the ferroelectric transition order so the ferroelectric transition in the film is still of the second order. For a second-order phase transition, a ferroelectric transition will take place when the following determinant is zero:

$$
\begin{vmatrix}
\dfrac{\partial^2 f}{\partial p_1^2} & \dfrac{\partial^2 f}{\partial p_1 \partial p_2} & \dfrac{\partial^2 f}{\partial p_1 \partial p_3} \\[2mm]
\dfrac{\partial^2 f}{\partial p_2 \partial p_1} & \dfrac{\partial^2 f}{\partial p_2^2} & \dfrac{\partial^2 f}{\partial p_2 \partial p_3} \\[2mm]
\dfrac{\partial^2 f}{\partial p_3 \partial p_1} & \dfrac{\partial^2 f}{\partial p_3 \partial p_2} & \dfrac{\partial^2 f}{\partial p_3^2}
\end{vmatrix}_{p_1=p_2=p_3=0} = 0. \tag{9}
$$

Let us first consider the situation that there is no AFD structural transition, i.e., $q_1=q_2=q_3=0$. The ferroelectric transition temperature can be determined from $T_c^F=\max[T_1^F,T_3^F]$, where T_1^F and T_3^F are, respectively, solutions to

$$
\alpha_1(T_1^F) + \Delta\alpha_1^f = \alpha_1(T_1^F) - \frac{(c_{11}-c_{12})(c_{11}+2c_{12})(Q_{11}+Q_{12})}{c_{11}} e_0
$$
$$
= 0 \tag{10}
$$

and
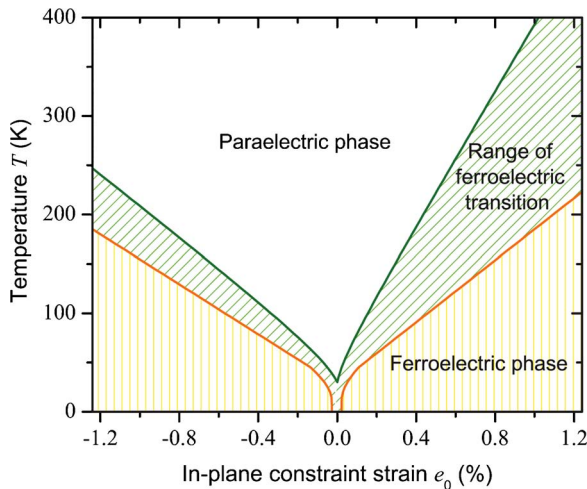
FIG. 1. (Color online) Ferroelectric transition temperature range vs in-plane substrate constraint strain in SrTiO₃ films without considering any preceding AFD structural transition.

TABLE I. Elastic stiffness in units of dyn/cm².

	Ref. 21	Ref. 21	Ref. 21	Refs. 16, 19, and 22–24
$c_{11}(\times10^{12})$	3.48	3.181	3.156	3.36
$c_{12}(\times10^{12})$	1.01	1.025	1.027	1.07
$c_{44}(\times10^{12})$	1.19	1.236	1.215	1.27

$$
\alpha_1(T_3^F) + \Delta\alpha_3^f = \alpha_1(T_3^F) - \frac{2(c_{11}-c_{12})(c_{11}+2c_{12})Q_{12}}{c_{11}} e_0 = 0. \tag{11}
$$

Therefore, it is easy to see that the ferroelectric transition temperature depends on the in-plane strain e_0, the elastic constants c_{ij}, the electrostrictive coefficients Q_{ij}, and the coefficient $\alpha_1(T)$. Different values for these parameters have, however, been reported in the literature by different groups. We list all that we consider to be the most accurate reported values[2,6,16,19,21–26] in Tables I–III, respectively. In this paper cgs units are used. Based on the spread in the reported values of these parameters, we calculate the ferroelectric transition temperature as a function of strain.

Figure 1 shows the possible ferroelectric transition temperatures as a function of the in-plane substrate constraint strain for $(100)_p$ SrTiO₃ thin films without considering any preceding AFD structural transition. The diagonally shaded regions indicate the range of ferroelectric transition temperatures due to the spread in the parameters entering in Eqs. (10) and (11). As has been shown previously in SrTiO₃ and other systems,[16,27] the ferroelectric transition temperature increases with increasing in-plane strain, irrespective of whether it is compressive or tensile. In the figure, the region labeled "paraelectric phase" means where $p_1=p_2=p_3=0$ and $q_1=q_2=q_3=0$, which will be used in the following figures.

B. Range of AFD structural transition temperature in SrTiO₃ films

The AFD structural transition temperature in strained $(100)_p$ SrTiO₃ films can be obtained in a similar way. If we ignore any possible preceding ferroelectric transition, the AFD structural transition temperature can be determined from $T_c^S=\max[T_1^S,T_3^S]$, where T_1^S and T_3^S are, respectively, the solutions to

$$
\beta_1(T_1^S) + \Delta\beta_1^f = \beta_1(T_1^S) - \frac{(c_{11}-c_{12})(c_{11}+2c_{12})(\Lambda_{11}+\Lambda_{12})}{c_{11}} e_0
$$
$$
= 0 \tag{12}
$$

and

TABLE II. Electrostrictive coefficients in units of cm⁴/esu².

	Refs. 16 and 22	Ref. 25	Ref. 25
$Q_{11}(\times10^{-13})$	5.09	8.90	7.34
$Q_{12}(\times10^{-13})$	−1.50	−1.67	−1.45
$Q_{44}(\times10^{-13})$	1.065		
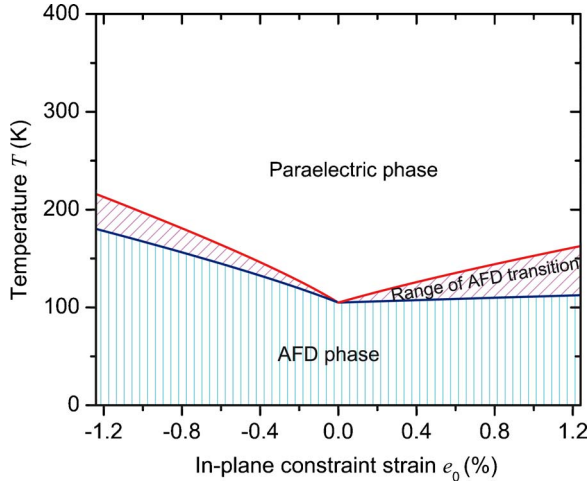
FIG. 2. (Color online) AFD structural transition temperature range vs in-plane substrate constraint strain in SrTiO$_3$ films without considering any preceding ferroelectric transition.

$$\beta_1(T_3^S) + \Delta\beta_3^f = \beta_1(T_3^S) - \frac{2(c_{11}-c_{12})(c_{11}+2c_{12})\Lambda_{12}}{c_{11}}e_0 = 0. \tag{13}$$

In the calculation, we used the Barrett formula, $\beta_1 = 1.32 \times 10^{26}[\coth(145/T) - \coth(145/105)]$, which was fitted to experiment data[28] and extrapolated to higher temperatures.[16] The values for the linear-quadratic coupling coefficients between the strain and structure order parameter, Λ_{ij}, from the literature[16,17,19,20,22,23,29] are listed in Table IV.

Based on Eqs. (12) and (13), and data in Table IV, we calculate the AFD structural transition temperatures as a function of in-plane strain. The results are presented in Fig. 2. It is shown that the AFD structural transition temperature also increases with increasing substrate in-plane constraint strain. The magnitude of the increase in the AFD structural transition temperature is less than that of the ferroelectric transition temperature. This is due to the weaker coupling between strain and the AFD structural order parameter as compared to that between strain and ferroelectricity. Therefore, it could be expected that under larger substrate constraint strains the ferroelectric phase transition would precede the AFD structural transition in biaxially constrained SrTiO$_3$ films. A recent experimental measurement[30,31] of the structural transitions in SrTiO$_3$ films showed that the increase in transition temperature due to the underlying substrate constraint is even higher than expected from thermodynamic analysis, indicating a possible underestimation in

TABLE III. Descriptions of α_1 in units of cm^2 dyn/esu^2 with temperature T in Kelvin.

$\alpha_1 = 4.5 \times 10^{-3}[\coth(54/T) - \coth(54/30)]$	Refs. 6, 16, and 22
$\alpha_1 = 6.98 \times 10^{-5}[42\coth(42/T) - 38]$, $T < 50$ K	Ref. 26
$\alpha_1 = 8.02 \times 10^{-5}(T - 28)$, $T > 70$ K	Ref. 26
$\alpha_1 = 7.86 \times 10^{-5}(T - 35.5)$, $T > 100$ K	Ref. 2

the literature of the coupling coefficient between strain and the AFD structural order parameter.

C. Effect of the AFD structural transition on the ferroelectric transition

From Figs. 1 and 2 it is clear that the AFD structural transition precedes the ferroelectric transition in constrained SrTiO$_3$ films when the in-plane substrate constraint strain is small. In this section, we will discuss the effect of the preceding AFD structural transition on the ferroelectric transition temperature. For the clarification of the following descriptions we listed in Table V all the possible stable phases in the biaxially strained $(100)_p$ SrTiO$_3$ films. In the designation of the table, the letters "**T**" and "**O**" indicate crystallographically "tetragonal" and "orthorhombic" symmetries, respectively. The superscript "P," "S" or "F" tells whether the phase is paraelectric, AFD structural (or ferroelastic) or ferroelectric. After the AFD structural transition from the paraelectric phase $\mathbf{T}^P$ to the ferroelastic phase $\mathbf{O}_1^S$ ($p_1 = p_2 = p_3 = 0$, $q_1 \neq 0$, $q_2 = q_3 = 0$), the ferroelectric transition temperature can be determined from $T_c^F = \max[T_1^F, T_2^F, T_3^F]$, where T_1^F, T_2^F, and T_3^F are the solutions of the following equations, respectively:

$$\alpha_1(T_1^F) + \Delta\alpha_1^f + (t_{11} + \Delta t_{11}^f)\frac{\beta_1 + \Delta\beta_1^f}{2(\beta_{11} + \Delta\beta_{11}^f)} = 0, \tag{14a}$$

$$\alpha_1(T_2^F) + \Delta\alpha_1^f + (t_{12} + \Delta t_{12}^f)\frac{\beta_1 + \Delta\beta_1^f}{2(\beta_{11} + \Delta\beta_{11}^f)} = 0, \tag{14b}$$

$$\alpha_1(T_3^F) + \Delta\alpha_3^f + (t_{12} + \Delta t_{31}^f)\frac{\beta_1 + \Delta\beta_1^f}{2(\beta_{11} + \Delta\beta_{11}^f)} = 0. \tag{14c}$$

If the ferroelastic phase is $\mathbf{T}^S$ ($p_1 = p_2 = p_3 = 0$, $q_1 = q_2 = 0$, $q_3 \neq 0$), the $T_1^F = T_2^F$ and T_3^F are solutions to

$$\alpha_1(T_1^F) + \Delta\alpha_1^f + (t_{12} + \Delta t_{13}^f)\frac{\beta_1 + \Delta\beta_3^f}{2(\beta_{11} + \Delta\beta_{33}^f)} = 0, \tag{15a}$$

$$\alpha_1(T_3^F) + \Delta\alpha_3^f + (t_{11} + \Delta t_{33}^f)\frac{\beta_1 + \Delta\beta_3^f}{2(\beta_{11} + \Delta\beta_{33}^f)} = 0. \tag{15b}$$

For the case where the stable ferroelastic phase is $\mathbf{O}_2^S$ ($p_1 = p_2 = p_3 = 0$, $q_1 = \pm q_2 \neq 0$, $q_3 = 0$), the T_1^F, T_2^F and T_3^F are determined through

$$\alpha_1(T_1^F) + \Delta\alpha_1^f + (\beta_1 + \Delta\beta_1^f)$$

$$\times \frac{(t_{11} + \Delta t_{11}^f) + (t_{12} + \Delta t_{12}^f) - \frac{1}{2}(t_{44} + \Delta t_{44}^f)}{2(\beta_{11} + \Delta\beta_{11}^f) + (\beta_{12} + \Delta\beta_{12}^f)} = 0, \tag{16a}$$

TABLE IV. Coefficients Λ_{ij} (cm^{-2}) and β_{ij} (dyn/cm^6).

	Refs. 16, 19, and 22	Refs. 17 and 23[a]	Ref. 29[a]	Ref. 20[a]
$\Lambda_{11}(\times 10^{14})$	8.7	14.7	9.32	8.35
$\Lambda_{12}(\times 10^{14})$	−7.8	−7.34	−6.40	−5.54
$\Lambda_{44}(\times 10^{14})$	−9.2	−9.88	−6.93	−7.56
$\beta_{11}(\times 10^{43})$	1.69	1.58	1.20	0.996
$\beta_{12}(\times 10^{43})$	3.88	3.78	2.88	2.72

[a]Indicates values derived with the elastic constants (Refs. 23 and 24) $c_{11}=3.36\times10^{12}$, $c_{12}=1.07\times10^{12}$, and $c_{44}=1.27\times10^{12}$ dyn/cm^2.

$$\alpha_1(T_2^F) + \Delta\alpha_1^f + (\beta_1 + \Delta\beta_1^f)$$

$$\times \frac{(t_{11} + \Delta t_{11}^f) + (t_{12} + \Delta t_{12}^f) + \frac{1}{2}(t_{44} + \Delta t_{44}^f)}{2(\beta_{11} + \Delta\beta_{11}^f) + (\beta_{12} + \Delta\beta_{12}^f)} = 0,$$

$$(16b)$$

$$\alpha_1(T_3^F) + \Delta\alpha_3^f + (\beta_1 + \Delta\beta_1^f)\frac{2(t_{12} + \Delta t_{31}^f)}{2(\beta_{11} + \Delta\beta_{11}^f) + (\beta_{12} + \Delta\beta_{12}^f)} = 0.$$

$$(16c)$$

Using the data listed in Table IV, numerical calculations show that the tetragonal $\mathbf{T}^S$ phase ($q_1=q_2=0$, $q_3\neq0$) is always stable when $e_0<0$. When $e_0>0$, however, the variation in the coefficients leads to either the orthorhombic $\mathbf{O}_1^S$ ($q_1\neq0$, $q_2=q_3=0$ or $q_2\neq0$, $q_1=q_3=0$) or $\mathbf{O}_2^S$ ($q_1=\pm q_2\neq0$, $q_3=0$) as the stable phase. It should be noted that the data in Table IV produce a stable tetragonal phase under the stress-free condition, in agreement with experiment.[3]

The available coupling coefficients t_{ij} between the polarization **p** and the structural order parameter **q** under stress-free conditions are listed in Table VI. Based on Eqs. (14)–(16) and the available data listed in Tables I–IV and VI, we recalculated the ferroelectric transition temperatures taking the possibility of a preceding AFD structural transition into account. The results are summarized in Fig. 3. In the figure, the vertically shaded regions represent the stable ferroelectric phase; the diagonally shaded regions show the uncertainty in the ferroelectric transition temperature due to the uncertainty of the parameters from different sources. The dash-dot lines indicate the boundaries of the AFD structural transition ranges from Fig. 2. The dashed lines show the boundaries of the range of ferroelectric transition temperatures without taking into account the effect of the possible AFD structural transition (from Fig. 1). It is easily seen that under a compressive substrate constraint, the ferroelectric transition is depressed when it follows an AFD structural transition, i.e., the ferroelectric transition temperature decreases due to a preceding AFD structural transition. Under a tensile substrate constraint, i.e., $e_0>0$, the ferroelectric transition temperature may be either enhanced or depressed slightly when it follows an AFD structural transition, depending on the stable AFD structural phase. The ferroelectric transition is depressed when it follows an AFD transition to $\mathbf{O}_2^S$ orthorhombic phase, while it may be enhanced when it

follows an AFD transition to $\mathbf{O}_1^S$ orthorhombic phase. The change in the ferroelectric transition temperature due to the preceding AFD phase is, however, very small under a tensile strain.

An earlier thermodynamic prediction[14] was a combination of Figs. 1 and 3, i.e., where the range of ferroelectric transition contained both without and with considering preceding AFD structural transitions. Moreover, it included an additional set of reported electrostrictive coefficients. This set was eliminated from the calculations leading to Figs. 1 and 3 after scrutinizing the experimental data. The area surrounded by lines with '×' in Fig. 3 is thus an updated prediction of the earlier diagram[14] that includes the uncertainty in the experimentally measured parameters that go into the thermodynamic analysis.

From Fig. 3, the predicted ferroelectric transition temperature ranges from 175 to 370 K as compared to the experimentally determined transition temperature (see the cross in Fig. 3) for the particular case of 0.94% tensile strain, i.e., the average strain of $\bar{\varepsilon}_{11}=0.936\%$ and $\bar{\varepsilon}_{22}=0.951\%$ of a 500-Å-thick $(100)_p$ SrTiO$_3$ film epitaxially grown with slight relaxation on a (110) DyScO$_3$ substrate.[14,15] Therefore, despite the error bars of the predicted transition temperature that arise from uncertainty in the coefficients, the agreement between prediction and experiment is considered to be excellent, and the high ferroelectric transition temperature is indeed largely due to the strain.
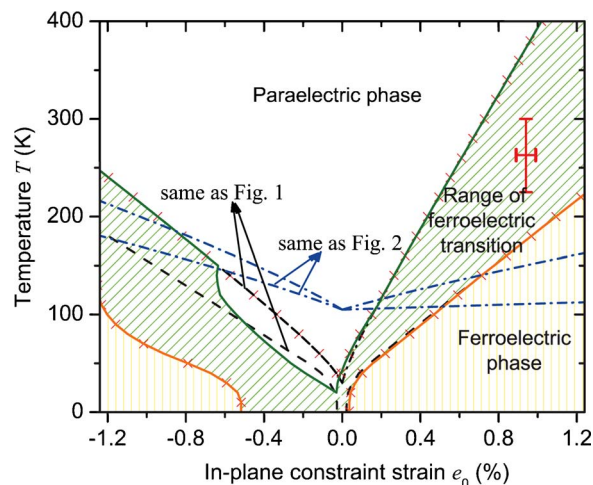
FIG. 3. (Color online) Ferroelectric transition temperature range vs in-plane substrate constraint strain in SrTiO$_3$ films after taking the AFD transition into consideration.

TABLE V. Phase definitions in biaxially strained $(100)_p$ SrTiO$_3$ films.

Designation	Point group symmetry	Order parameter $(\mathbf{p};\mathbf{q})$ (with respect to the pseudocubic cell)	Equivalent domain variants (with respect to the pseudocubic cell)
$\mathbf{T}^P$	$4/mmm$	$(0,0,0;0,0,0)_p$	
$\mathbf{T}^S$	$4mm$	$(0,0,0;0,0,q_3)_p$	$(0,0,0;0,0,-q_3)_p$
$\mathbf{O}_1^S$	$mm2$	$(0,0,0;q_1,0,0)_p$	$(0,0,0;-q_1,0,0)_p$, $(0,0,0;0,q_1,0)_p$, $(0,0,0;0,-q_1,0)_p$
$\mathbf{O}_2^S$	$mm2$	$(0,0,0;q_1,q_1,0)_p$	$(0,0,0;-q_1,q_1,0)_p$, $(0,0,0;q_1,-q_1,0)_p$, $(0,0,0;-q_1,-q_1,0)_p$
$\mathbf{T}_1^F$	$4mm$	$(0,0,p_3;0,0,0)_p$	$(0,0,-p_3;0,0,0)_p$
$\mathbf{O}_1^F$	$mm2$	$(p_1,0,0;0,0,0)_p$	$(-p_1,0,0;0,0,0)_p$, $(0,p_1,0;0,0,0)_p$, $(0,-p_1,0;0,0,0)_p$
$\mathbf{O}_2^F$	$mm2$	$(p_1,p_1,0;0,0,0)_p$	$(-p_1,p_1,0;0,0,0)_p$, $(p_1,-p_1,0;0,0,0)_p$, $(-p_1,-p_1,0;0,0,0)_p$
$\mathbf{T}_2^F$	$4mm$	$(0,0,p_3;0,0,q_3)_p$	$(0,0,-p_3;0,0,q_3)_p$, $(0,0,p_3;0,0,-q_3)_p$, $(0,0,-p_3;0,0,-q_3)_p$
$\mathbf{O}_3^F$	$mm2$	$(p_1,0,0;0,q_2,0)_p$	$(-p_1,0,0;0,q_2,0)_p$, $(p_1,0,0;0,-q_2,0)_p$, $(-p_1,0,0;0,-q_2,0)_p$, $(0,p_1,0;q_2,0,0)_p$, $(0,-p_1,0;q_2,0,0)_p$, $(0,p_1,0;-q_2,0,0)_p$, $(0,-p_1,0;-q_2,0,0)_p$
$\mathbf{O}_4^F$	$mm2$	$(p_1,0,0;0,0,q_3)_p$	$(-p_1,0,0;0,0,q_3)_p$, $(p_1,0,0;0,0,-q_3)_p$, $(-p_1,0,0;0,0,-q_3)_p$, $(0,p_1,0;0,0,q_3)_p$, $(0,-p_1,0;0,0,q_3)_p$, $(0,p_1,0;0,0,-q_3)_p$, $(0,-p_1,0;0,0,-q_3)_p$
$\mathbf{O}_5^F$	$mm2$	$(p_1,p_1,0;0,0,q_3)_p$	$(p_1,p_1,0;0,0,-q_3)_p$, $(-p_1,p_1,0;0,0,q_3)_p$, $(-p_1,p_1,0;0,0,-q_3)_p$, $(p_1,-p_1,0;0,0,q_3)_p$, $(p_1,-p_1,0;0,0,-q_3)_p$, $(-p_1,-p_1,0;0,0,q_3)_p$, $(-p_1,-p_1,0;0,0,-q_3)_p$
$\mathbf{O}_6^F$	$mm2$	$(p_1,p_1,0;q_1,q_1,0)_p$	$(-p_1,-p_1,0;q_1,q_1,0)_p$, $(p_1,p_1,0;-q_1,-q_1,0)_p$, $(-p_1,-p_1,0;-q_1,-q_1,0)_p$, $(p_1,-p_1,0;q_1,-q_1,0)_p$, $(p_1,-p_1,0;-q_1,-q_1,0)_p$, $(-p_1,p_1,0;q_1,q_1,0)_p$, $(-p_1,p_1,0;q_1,-q_1,0)_p$

D. Temperature-constraint strain phase diagrams

A plot of the relative stability of various structural and ferroelectric states as a function of strain is called a stability diagram. Figures 4(a) and 4(b) present two stability diagrams for $(100)_p$ SrTiO$_3$ thin films. Table VII lists the values of the coefficients used for the phase diagram calculation, and most of them were also used by Pertsev, Tagantsev, and Setter[16] and Tagantsev, Courtans, and Arzel.[22] The stable phase under a given temperature and in-plane strain was obtained by minimizing the total energy with respect to the polarization and the structural order parameter. In the figures, the paraelectric phase means that $p_1=p_2=p_3=q_1=q_2=q_3=0$, as in Figs. 1–3. The other notations indicate the nonzero components of the polarization and the AFD structural order parameter of the stable phases in the corresponding regions. The solid lines represent the phase boundaries where adjacent phases have equal energies. It is seen that the pure ferroelectric phase (i.e., $q_1=q_2=q_3=0$) or pure AFD structural phase (i.e., $p_1=p_2=p_3=0$) may be stabilized under certain temperature and constraint strains. The differences between Figs. 4(a) and 4(b) arise solely from the different value of the coefficient α_{12} in the Landau free energy, i.e., $\alpha_{12}=5.5$

$\times 10^{-12}$ cm^6 dyn/esu^4 for Fig. 4(a) and $\alpha_{12}=1.7\times 10^{-12}$ cm^6 dyn/esu^4 for Fig. 4(b). The value of $\alpha_{12}=5.5 \times 10^{-12}$ cm^6 dyn/esu^4 is the average of the experimental data[32] $\alpha_{12}=9.28\times 10^{-12}$ cm^6 dyn/esu^4 at $T=8$ K and the $\alpha_{12}=1.7\times 10^{-12}$ cm^6 dyn/esu^4 value used in the previous calculation.[22] It is seen that the variation in the Landau coefficients (in this case the values for α_{12}) from different sources will result in different stable states for the ferroelectric phase. For example, under tensile strain the larger α_{12} value stabilizes the ferroelectric $\mathbf{O}_1^F$ or $\mathbf{O}_3^F$ phase (i.e., $p_1 \neq 0$, $p_2=p_3=0$ or $p_2 \neq 0$, $p_1=p_3=0$) [see Fig. 4(a)], but the smaller α_{12} value favors the ferroelectric $\mathbf{O}_2^F$ or $\mathbf{O}_6^F$ phase (i.e., $p_1=\pm p_2$, $p_3=0$) [see Fig. 4(b)]. The stability diagram in Fig. 4(b) is essentially the same as that published earlier by Pertsev, Tagantsev, and Setter.[16]

E. Ferroelectric domain morphologies

It should be emphasized that the domain stability maps in Fig. 4 were constructed by assuming a homogeneous single domain for each phase. During a structural or ferroelectric phase transition, it is inevitable that multiple domains or het-
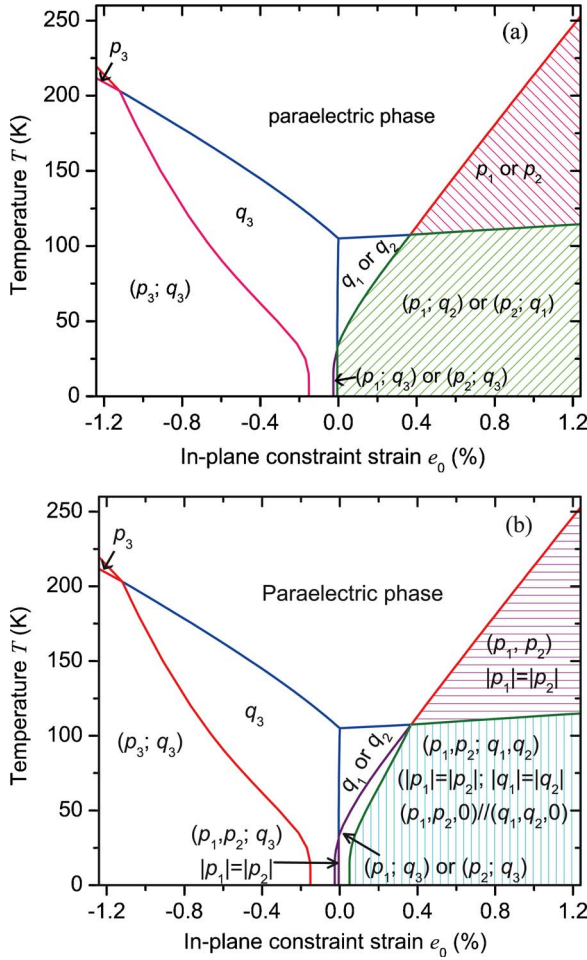
FIG. 4. (Color online) Phase stability diagram of $(100)_p$-oriented single-domain SrTiO$_3$ films by taking (a) $\alpha_{12}=5.5 \times 10^{-12}$ cm^6 dyn/esu^4; (b) $\alpha_{12}=1.7\times 10^{-12}$ cm^6 dyn/esu^4.

FIG. 5. (Color online) Ferroelectric domain morphology at $T = 125$ K and $e_0=0.94\%$ obtained by taking $\alpha_{12}=5.5 \times 10^{-12}$ cm^6 dyn/esu^4 and (a) considering dipole-dipole interaction, (b) ignoring dipole-dipole interaction. The polarization vectors **p** of the domains are indicated by the arrows. The slab underlying the film is the substrate.

erophase structures form due to the degeneracy of domain states and the release of strain energy. To predict the domain structures, we employed the phase-field model for ferroelectric thin films.[33,34] The temporal and spatial evolutions of the two order parameters **p** and **q** are described by the time dependent Ginzburg-Landau equations: $\partial p_i(\mathbf{x},t)/\partial t = -L_p\delta F/\delta p_i(\mathbf{x},t)$, $\partial q_i(\mathbf{x},t)/\partial t = -L_q\delta F/\delta q_i(\mathbf{x},t)$, $(i=1,2,3)$ where L_p and L_q are the kinetic coefficients related to the domain mobilities of **p** and **q**, respectively. F is the total free energy of the system, including the bulk free energy, elastic deformation energy, dipole-dipole interaction energy, and domain wall energy, i.e.

	Ref. 16	Ref. 22
$t_{11}(\times 10^{15})$	−2.34	−1.94
$t_{12}(\times 10^{15})$	−0.94	−0.84
$t_{44}(\times 10^{15})$	6.51	6.51

$$F = \int \int_V \int [f_{bulk}(p_i,q_i) + f_{elastic}(p_i,q_i,\varepsilon_{ij}) + f_{electric}(p_i,E_i)$$
$$+ f_{wall}(p_{i,j},q_{i,j})]d^3x,$$

where V is the volume of the film and $d^3x=dx_1dx_2dx_3$. In simulations we assume that the strain field ε_{ij} and electric field E_i are always at equilibrium for a given distributions of **p** and **q**. The calculations of the elastic energy and the electric energy can be found elsewhere.[34,35] For an isotropic system, the domain wall energy is calculated through $f_{wall} = (G_p p_{i,j}p_{i,j}+G_q q_{i,j}q_{i,j})/2$, where G_p and G_q are the domain wall energy coefficients and $p_{i,j}=\partial p_i/\partial x_j$, $q_{i,j}=\partial q_i/\partial x_j$. A model size of $128\Delta x\times 128\Delta x\times 36\Delta x$ was employed, and periodic boundary conditions were applied along the x_1 and x_2 axes. Δx is the grid spacing. The thickness of the film was taken as $20\Delta x$. In simulation, $L_q/L_p=180$, $G_q/G_p=0.012$, and $G_p/G_0=0.4$ where G_0 is related to the magnitude of Δx through $\Delta x=\sqrt{G_0/\alpha_0}$ and $\alpha_0=|\alpha_1|$. The corresponding ferroelectric domain wall thickness is about $1.5\Delta x$.

1. Orthorhombic $\mathbf{O}_1^F$, $\mathbf{O}_3^F$, and $\mathbf{O}_1^S$ domain morphologies

Using the set of parameters corresponding to Fig. 4(a), the predicted orthorhombic $\mathbf{O}_1^F$ domain morphology at $T = 125$ K and $e_0=0.94\%$ is shown in Fig. 5. Figure 6 depicts the orthorhombic $\mathbf{O}_1^S$ domain morphology at $T=100$ K and $e_0=0.2\%$. Due to the uniform biaxial tensile strain, the order parameters **p** or **q** of the stable phases are all in plane and lie along the $\langle 100\rangle_p$ directions. The four colors used to depict
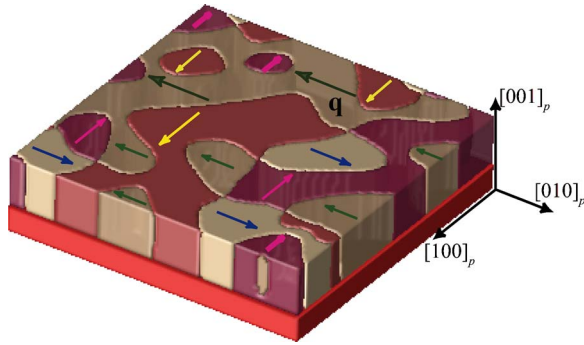
FIG. 6. (Color online) AFD structural domain morphology at $T=100$ K and $e_0=0.2\%$. The order parameter vectors **q** of the domains are indicated by the arrows.

the films in Figs. 5 and 6 represent, respectively, the four variants, i.e., $(p_1,0,0)/(q_1,0,0)$, $(-p_1,0,0)/(-q_1,0,0)$, $(0,p_1,0)/(0,q_1,0)$, and $(0,-p_1,0)/(0,-q_1,0)$. The directions of the corresponding order parameter vector **p** or **q** on the variants are shown by the arrows. From the figures it is seen that both the ferroelectric and AFD structural domain microstructures contain both 90° and 180° domain walls. The 90° domain walls, which release the strain energy, are basically normal to $\langle 110 \rangle_p$ in-plane directions. Moreover, the domain volume fractions of the variants $(\pm p_1,0,0)/(\pm q_1,0,0)$ and $(0,\pm p_1,0)/(0,\pm q_1,0)$ are about the same, which is compatible with the uniform biaxial constraint. The ferroelectric domains obtained by considering dipole-dipole interactions have sharp wedge shapes. In contrast, the domain walls of the AFD structural domains (Fig. 6) and the ferroelectric domains without dipole-dipole interactions [Fig. 5(b)] appear to be more rounded. Dipole-dipole interactions were taken into account for the following presented results.

We also simulated the case where both the ferroelectric polarization **p** and the AFD structural order parameter **q** are simultaneously nonzero, i.e., phase O_3^F. The domain morphologies obtained at $T=100$ K and $e_0=0.94\%$ are given in Figs. 7(a) and 7(b) for the order parameters **p** and **q**, respectively. It is found that the morphology of **p** in Fig. 7(a) is similar to that of a pure ferroelectric phase shown in Fig. 5(a). Most interesting is the fact that the domain shapes of the AFD structural variants $(\pm q_2,0,0)$ and the ferroelectric variants $(0,\pm p_1,0)$ are almost exactly the same, and so are the AFD structural variants $(0,\pm q_2,0)$ and the ferroelectric variants $(\pm p_1,0,0)$. This is consistent with the prediction shown in the phase diagram where $(p_1,0,0;0,q_2,0)$ or $(0,p_1,0;q_2,0,0)$ is the stable phase for this particular temperature and constraint strain. It implies that the polarization vector **p** is always perpendicular to the AFD structural displacement vector **q**. Moreover, the domain shape of **q** is not as rounded as that in Fig. 6 and there are more 180° antiphase domain walls for **q** than for **p**. They should be attributed to the interactions between the two order parameters **p** and **q**, i.e., they have to be paired to each other which might slow down the evolution of the AFD domains compared to the pure ferroelastic phase.

2. Orthorhombic O_6^F domain morphology

If we employ the set of coefficients which produced the domain stability map shown in Fig. 4(b), the stable ferroelec-
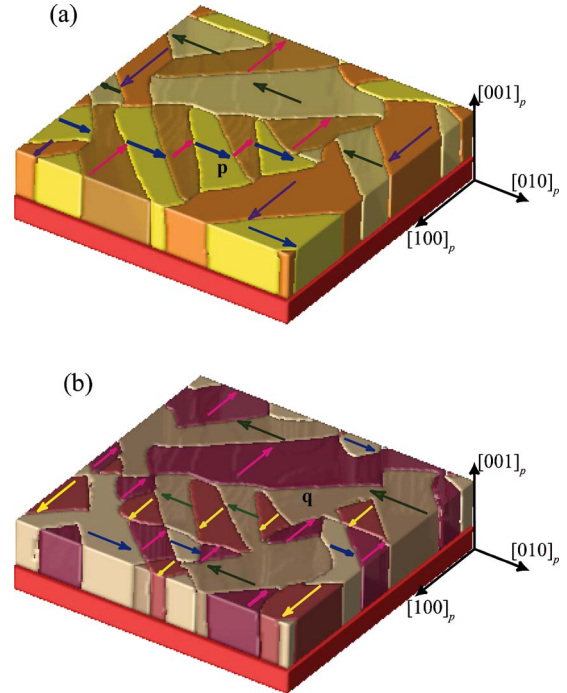
FIG. 7. (Color online) (a) Ferroelectric domain morphology and (b) AFD structural domain morphology at $T=100$ K and $e_0=0.94\%$ obtained by taking $\alpha_{12}=5.5\times10^{-12}$ cm⁶ dyn/esu⁴. The directions of the vectors **p** and **q** in the corresponding domains are shown by the arrows.

tric phase for the case of $T=100$ K and $e_0=0.94\%$ is the orthorhombic phase O_6^F. The corresponding morphology is shown in Fig. 8. In the orthorhombic phase, both the ferroelectric polarization **p** and the AFD structural order parameter vector **q** lie in plane and are along the $\langle 110 \rangle_p$ directions. From the domain morphologies it is evident that the polarization **p** and the AFD order parameter **q** are always parallel to each other, in contrast to those shown in Fig. 7, where **p** and **q** are orthogonal to each other. The 90° domain walls having orientations of $\{100\}_p$ or $\{010\}_p$ are clearly seen in Fig. 8.

F. Experimental determination of the ferroelectric state

1. Optical second harmonic generation (SHG) measurement

To determine the point group symmetry and the direction of the ferroelectric polarization in a strained $(100)_p$ SrTiO₃ film on a (110) DyScO₃ substrate $(e_0=0.94\%)$,[14,15] we employed optical SHG measurements. SHG involves the conversion of light at frequency ω into an optical signal at a frequency of 2ω by a nonlinear material. The conversion process occurs by the creation of a nonlinear polarization $p_i^{2\omega}\propto d_{ijk}E_j^\omega E_k^\omega$, by light of frequency ω through the third order nonlinear tensor d_{ijk}. Each of the subscripts i, j, k refers to any one of the crystal physics axes of the material, 1, 2, 3. Anticipating a little, the strained SrTiO₃ has point group symmetry $mm2$, where the twofold rotation axis lies within the plane of the SrTiO₃ thin film. By symmetry considerations, the ferroelectric polarization **p** in this point group can

(a)

(b)
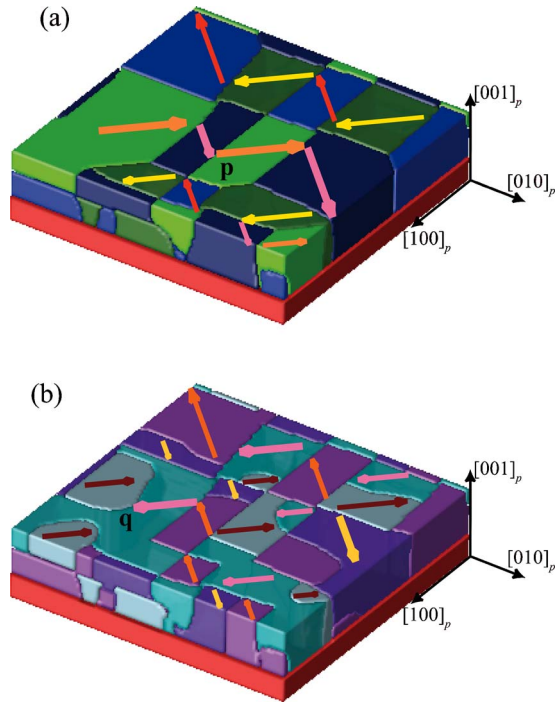
FIG. 8. (Color online) (a) Ferroelectric domain morphology and (b) AFD structural domain morphology at $T=100$ K and $e_0 =0.94\%$ obtained by taking $\alpha_{12}=1.7\times10^{-12}$ cm^6 dyn/esu^4. The directions of the vectors **p** and **q** in the domains are shown by the arrows.

lie only along this twofold axis, which is conventionally labeled as crystal physics axis x_3. Additionally, by Neumann's law, only the nonlinear coefficients, d_{15}, d_{24}, d_{31}, d_{32}, and d_{33} are nonzero, where the abbreviated Voigt's notation of $jk \rightarrow l$ is used for these third-rank coefficients. In the tetragonal $4mm$, the same coefficients are non-zero, with the additional constraints of $d_{15}=d_{24}$ and $d_{31}=d_{32}$.

For a strained $(100)_p$ SrTiO$_3$ film on a (110) DyScO$_3$ substrate, we considered two possible models for the possible directions of polarization in the growth plane: **Model I**: the polarization appears along the $x[110]_p$ or $y[\bar{1}10]_p$ directions, the orthorhombic state; **Model II**: the polarization lies along the $x'[010]_p$ or $y'[100]_p$ directions, the tetragonal state.

The SHG experiment was performed as follows. A beam of light (the fundamental wave) with wavelength 800 nm was incident from the substrate side in normal geometry, and its polarization direction, at an angle θ from the y axis, was rotated continuously within the plane of the film. The same 500-Å-thick strained SrTiO$_3$ film grown on (110) DyScO$_3$ studied previously[14,15] was used here. The intensity, $I_j^{2\omega}$, of the output SHG signal at 400 nm wavelength from the film was detected along either $j=x,y,x',y'$ polarization directions by a photomultiplier tube. The resulting polar plots of SHG intensity at 223 K are shown in Fig. 9. A reference study of a bare (110) DyScO$_3$ substrate without any film yielded no SHG intensity within the detection limits. A theoretical analysis of this film system, similar to that outlined in other references,[36–42] yields the following expression for the SHG intensity:

$$I_j^{2\omega} = K_{1,j}\sin^2 2\theta + K_{2,j}(\sin^2\theta + K_{3,j}\cos^2\theta)^2$$
$$+ K_{4,j}(\sin^2\theta + K_{3,j}\cos^2\theta)\sin 2\theta, \qquad (17)$$

where $K_{i,j}$ are constants. We now explore each of the two possible models for the polarization directions.

Model I: Assuming that the domain polarizations are along the pseudo-cubic $x[110]_p$ or $y[\bar{1}10]_p$ directions, it can be shown[43] that

$$\frac{d_{33}}{d_{31}} = K_{3,y} = (K_{3,x})^{-1}. \qquad (18)$$

From Eq. (17), we can deduce that $(K_{3,j})^2 =I_j^{2\omega}(0°)/I_j^{2\omega}(90°)$. Further, condition (18) stipulates that $K_{3,x}=K_{3,y}^{-1}$, which therefore requires that

$$I_x^{2\omega}(90°)/I_x^{2\omega}(0°) = I_y^{2\omega}(0°)/I_y^{2\omega}(90°). \qquad (19)$$

As seen from Figs. 9(a) and 9(b), this condition is clearly experimentally satisfied. At -50 °C (223 K), the experimental values are $I_x^{2\omega}(90°)/I_x^{2\omega}(0°)\sim(1.58)^2$ and $I_y^{2\omega}(0°)/I_y^{2\omega}(90°)\sim(1.48)^2$. From Eqs. (18) and (19), we therefore get a resultant value of $d_{33}/d_{31}=1.53\pm0.05$ at 223 K.

Model II: Assuming that the ferroelectric polarization may be along $x'[100]_p$ and $y'[010]_p$ directions, and performing a similar analysis as above,[43] we arrive at the required stipulation that

TABLE VII. Parameters of cubic SrTiO$_3$ under stress free conditions at low temperatures in cgs units.

$\alpha_1=4.5\times10^{-3}[\coth(54/T)-\coth(54/30)]$	$\beta_1=1.32\times10^{26}[\coth(145/T)-\coth(145/105)]$
$\alpha_{11}=2.1\times10^{-12}$	$\beta_{11}=1.69\times10^{43}$
$\alpha_{12}=5.5\times10^{-12}/\alpha_{12}=1.7\times10^{-12}$	$\beta_{12}=3.88\times10^{43}$
$Q_{11}=5.09\times10^{-13}$	$\Lambda_{11}=8.7\times10^{14}$
$Q_{12}=-1.50\times10^{-13}$	$\Lambda_{12}=-7.8\times10^{14}$
$Q_{44}=1.065\times10^{-13}$	$\Lambda_{44}=-9.2\times10^{14}$
$c_{11}=3.36\times10^{12}$	$t_{11}=-1.94\times10^{15}$
$c_{12}=1.07\times10^{12}$	$t_{12}=-0.84\times10^{15}$
$c_{44}=1.27\times10^{12}$	$t_{44}=6.51\times10^{15}$
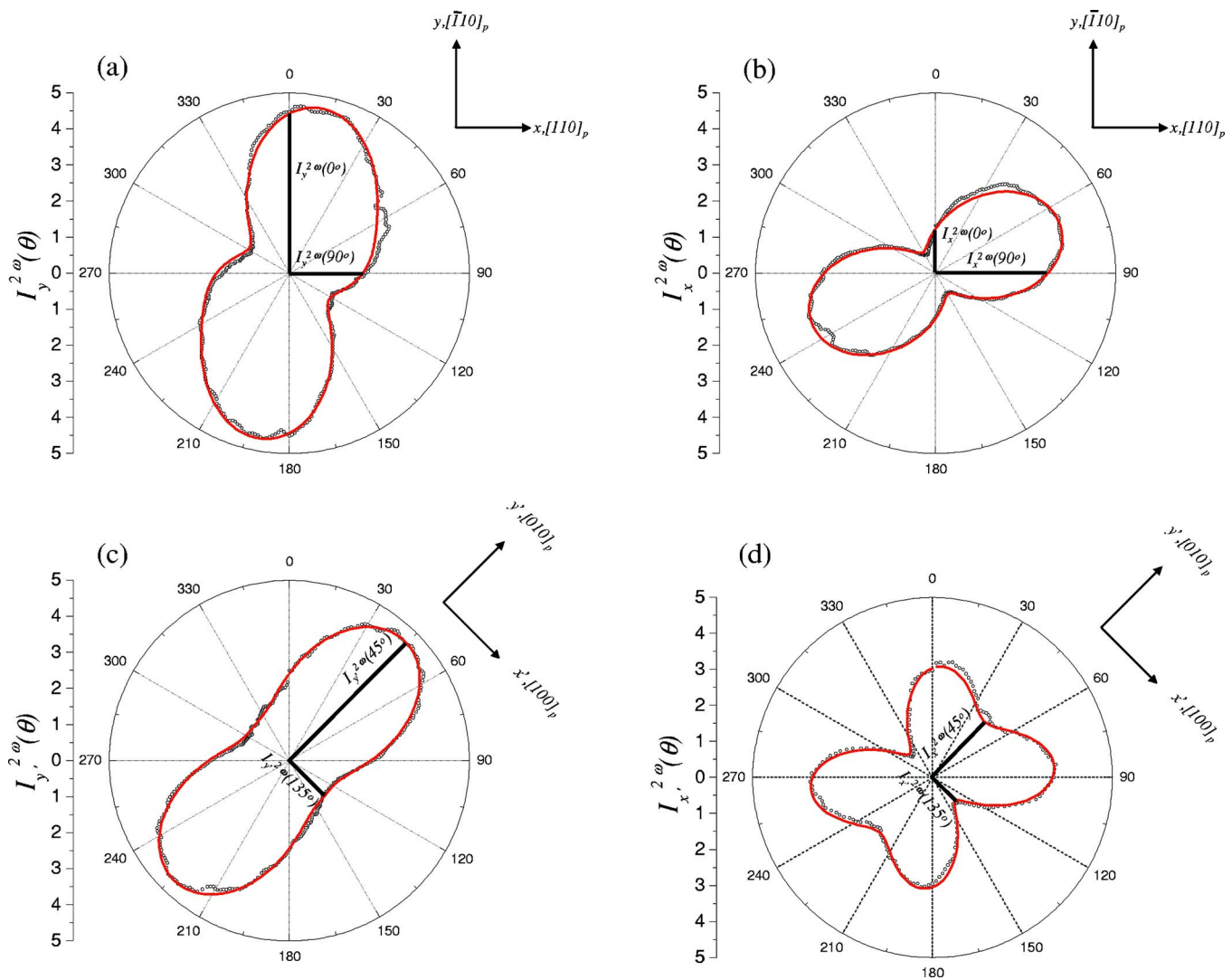
FIG. 9. (Color online) Polar plots of second harmonic generation intensity ($I_j^{2\omega}$) at $T=223$ K as a function of the polarization angle, θ, of the fundamental light at frequency ω incident normal to the film surface of a 500-Å-thick SrTiO$_3$ film on (110) DyScO$_3$. (a) $I_y^{2\omega}$, (b) $I_x^{2\omega}$, (c) $I_{y'}^{2\omega}$, and (d) $I_{x'}^{2\omega}$, where directions x, y, x', and y', are defined in the inset. The circles are the measured data and the solid curves are the theoretical fits based on Eq. (17).

$$I_{x'}^{2\omega}(135°)/I_{x'}^{2\omega}(45°)=I_{y'}^{2\omega}(45°)/I_{y'}^{2\omega}(135°). \qquad (20)$$

Figures 9(c) and 9(d) show the polar plots of SHG intensity $I_j^{2\omega}$, where $j=x'[100]_p$ and $y'[010]_p$, respectively. It is seen that condition (20) is *not* satisfied; the left hand argument of Eq. (20) is equal to ~0.42 and the right hand side of Eq. (20) is equal to ~3.36.

The above experimental conclusions were also confirmed to be true for a series of temperatures from 77 to 300 K, and will be reported separately.[43] From the above discussion, we conclude that **Model I** is correct, namely, that the point group symmetry of SrTiO$_3$ strained with $e_0=0.94\pm0.05\%$ in plane is $mm2$, and that the polarization lies along the pseudocubic $\langle 110 \rangle_p$ in-plane directions of the SrTiO$_3$ film. The results are consistent with a recent first-principles calculation which showed that the stable ferroelectric state is orthorhombic with point group $mm2$ (and space group $Amm2$) under a tensile strain.[44]

2. Confocal scanning optical microscopy (CSOM)

The electro-optic response of a 250-Å-thick $(100)_p$ SrTiO$_3$ film grown on (110) DyScO$_3$ was measured at room temperature (21 °C) using the confocal scanning optical microscopy (CSOM).[12] Four-circle x-ray diffraction measurements reveal that this thinner SrTiO$_3$ film is commensurately strained to the (110) DyScO$_3$ with an average biaxial strain of $e_0=1.16\pm0.05\%$. Interdigitated electrodes were deposited so that in-plane electric fields can be applied to the sample. The electrodes were arranged along several different angles with respect to the crystallographic axes. Light from a mode-locked Ti:sapphire laser (power=10 mW, wavelength ~820 nm) was focused with a microscope objective between two adjacent electrodes separated by 6 μm. A combined dc +ac voltage (frequency $f=85$ kHz) was applied to the electrodes. The reflected light was detected with an optical bridge using a portion of the incident beam for balancing. The Fresnel reflection ratio of the film changes as a result of
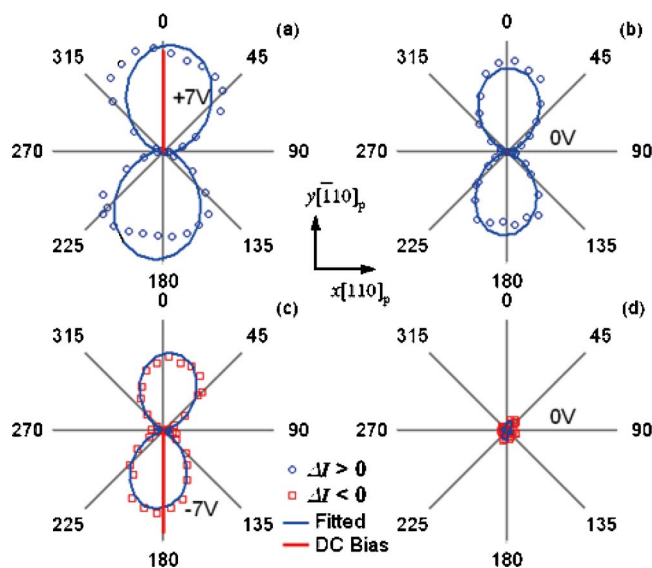
FIG. 10. (Color online) Electro-optic response of a 250-Å-thick SrTiO₃ film on (110) DyScO₃ as a function of light polarization angle and applied electric field in the pseudo-*y* direction at room temperature. Open circles and squares are experiment data. The solid curves represent linear least-square fits to Eq. (21). The thicker straight bars represent the applied voltage. Radial scales are in arbitrary units. V_{dc} was applied in the order of (a), (b), (c), and (d).

the electro-optic effect. After photodetection, a lock-in amplifier measures the light intensity variation ΔI as a function of the light polarization and applied dc bias. ΔI is proportional to the effective linear electro-optic coefficient[12] and can be fitted to the following equation:

$$\Delta I = a + b\cos(2\theta) + c\sin(2\theta), \qquad (21)$$

where θ is the light polarization angle; a, b and c are coefficients related to the linear electro-optic tensor.

Figure 10 shows the electro-optic effect with electric field along the $y[\bar{1}10]_p$ direction. The open circles and squares are the measured ΔI for light polarized in the corresponding direction. The dc bias voltages are labeled next to each plot and were applied in the clockwise order ($a \rightarrow b \rightarrow c \rightarrow d$). In (c-d), squares are used to represent negative values for ΔI. The light polarization dependent electro-optic effect originates from sample's birefringence and nonlinear optical properties. The electro-optic effect is generally stronger at higher bias fields and weaker at lower bias fields, and exhibits clear hysteresis [see Figs. 10(b) and 10(d)].

One possible interpretation for the field dependence of the electro-optic effect is that there are multiple ferroelectric nanodomains coexisting within the area of the diffraction-limited optical spot. At low field strengths, the domains with opposing polarization orientation mostly cancel. When the applied dc field is sufficiently strong, they polarize in the same direction and result in a saturated electro-optic effect. Further optical studies capable of revealing the nanoscale structure are necessary to provide direct support for this interpretation.

IV. CONCLUSIONS

The range of possible ferroelectric transition temperatures and the possible ferroelectric states of strained SrTiO₃ films were predicted using the reported properties of bulk SrTiO₃ single crystals. The ferroelectric transition temperature depends more strongly on the strain imposed by a substrate than does the AFD structural transition temperature, and hence the ferroelectric transition always precedes the AFD structural transition under a sufficiently large substrate constraint strain. Although the ferroelectric polarization is along the $[001]_p$ direction under a compressive biaxial strain, it could be along either $\langle 001 \rangle_p$ or $\langle 110 \rangle_p$ in-plane directions under a tensile strain, depending on which reported coefficients are used. Our experimental measurement of the polarization direction in a strained SrTiO₃ film under a larger tensile strain using both SHG and CSOM demonstrated that the ferroelectric polarization is along the $\langle 110 \rangle_p$ in-plane directions. It is found that the ferroelectricity in strained epitaxial SrTiO₃ thin films can be significantly depressed when the film is under compressive strain and the ferroelectric state is preceded by an AFD structural transition while the ferroelectric transition can take place at a higher temperature than the AFD structural transition when the film is under a larger tensile strain. Finally, the ferroelectric and structural domain morphologies were predicted using phase-field simulations, and it is shown that both the elastic interactions and the electrostatic interactions play an important role in determining the domain shapes and domain-wall orientations. The range in reported values for the bulk properties of SrTiO₃ single crystals and in the Landau coefficients lead to not only a relatively wide range of possible ferroelectric transition temperatures for a given strain, but also to different ferroelectric states and thus different domain structures at a biaxial tensile strain. The ferroelectric state found near room temperature in SrTiO₃ films strained in tension with $e_0 = 0.94\%$ is consistent with our calculations.

*Electronic address: yulan@lanl.gov

[1] R. C. Neville, B. Hoeneisen, and C. A. Mead, J. Appl. Phys. **43**, 2124 (1972).

[2] K. A. Müller and H. Burkard, Phys. Rev. B **19**, 3593 (1979).

[3] H. Unoki and T. Sakudo, J. Phys. Soc. Jpn. **23**, 546 (1967).

[4] P. A. Fleury, J. F. Scott, and J. M. Worlock, Phys. Rev. Lett. **21**, 16 (1968).

[5] H. Vogt, Phys. Rev. B **51**, 8046 (1995).

[6] A. Yamanaka, M. Kataoka, Y. Inaba, K. Inoue, B. Hehlen, and E. Courtens, Europhys. Lett. **50**, 688 (2000).

[7] W. Zhong and D. Vanderbilt, Phys. Rev. Lett. **74**, 2587 (1995).

[8] R. Martonák and E. Tosatti, Phys. Rev. B **49**, 12596 (1994).

[9] *Landolt-Börnstein: Numerical Data and Functional Relationships in Science and Technology*, edited by K.-H. Hellwege and A. M. Hellwege, Landolt-Börnstein, New Series, Group III, Vol. 16a (Springer, Berlin, 1981), p. 67.

[10] S. P. Alpay, I. B. Misirlioglu, V. Nagarajan, and R. Ramesh, Appl. Phys. Lett. **85**, 2044 (2004).

[11] V. Nagarajan, C. L. Jia, H. Kohlstedt, R. Waser, I. B. Misirlioglu, S. P. Alpay, and R. Ramesh, Appl. Phys. Lett. **86**, 192910 (2005).

[12] C. Hubert, J. Levy, A. C. Carter, W. Chang, S. W. Kiechoefer, J. S. Horwitz, and D. B. Chrisey, Appl. Phys. Lett. **71**, 3353 (1997).

[13] S. Tinte, M. G. Stachiotti, S. R. Phillpot, M. Sepliarsky, D. Wolf, and R. L. Migoni, J. Phys.: Condens. Matter **16**, 3495 (2004).

[14] J. H. Haeni, P. Irvin, W. Chang, R. Uecker, P. Reiche, Y. L. Li, S. Choudhury, W. Tian, M. E. Hawley, B. Craigo, A. K. Tagantsev, X. Q. Pan, S. K. Streiffer, L. Q. Chen, S. W. Kirchoefer, J. Levy, and D. G. Schlom, Nature (London) **430**, 758 (2004).

[15] Subsequent analysis of the 500-Å-thick $SrTiO_3$ film grown on (110) $DyScO_3$ discussed in Ref. 14 reveals that its biaxial strain state is more accurately given by $e_{11}=0.936\pm0.05\%$ and $e_{22}=0.951\pm0.05\%$. This corresponds to an average biaxial strain of $e_0=0.94\pm0.05\%$. S. K. Streiffer and M. D. Biegalski (private communication).

[16] N. A. Pertsev, A. K. Tagantsev, and N. Setter, Phys. Rev. B **61**, R825 (2000); **65**, 219901(E) (2002).

[17] J. C. Slonczewski and H. Thomas, Phys. Rev. B **1**, 3599 (1970).

[18] D. Fuchs, C. W. Schneider, R. Schneider, and H. Rietschel, J. Appl. Phys. **85**, 7362 (1999).

[19] H. Uwe and T. Sakudo, Phys. Rev. B **13**, 271 (1976).

[20] B. Pietrass, Phys. Status Solidi B **47**, 495 (1971).

[21] *Landolt-Börnstein: Numerical Data and Functional Relationships in Science and Technology*, edited by K.-H. Hellwege and A. M. Hellwege, Landolt-Börnstein, New Series, Group III (Ref. 9), p. 64.

[22] A. K. Tagantsev, E. Courtens, and L. Arzel, Phys. Rev. B **64**, 224107 (2001).

[23] J. C. Slonczewski, Phys. Rev. B **2**, 4646 (1970).

[24] R. O. Bell and G. Rupprecht, Phys. Rev. **129**, 90 (1963).

[25] *Landolt-Börnstein: Numerical Data and Functional Relationships in Science and Technology*, edited by K.-H. Hellwege and A. M. Hellwege, Landolt-Börnstein, New Series, Group III, Vol. 11 (Springer, Berlin, 1979), p. 418.

[26] *Landolt-Börnstein: Numerical Data and Functional Relationships in Science and Technology*, edited by K.-H. Hellwege and A. M. Hellwege, Landolt-Börnstein, New Series, Group III (Ref. 9), p. 60.

[27] N. A. Pertsev, A. G. Zembilgotov, and A. K. Tagantsev, Phys. Rev. Lett. **80**, 1988 (1998).

[28] K. A. Muller, in *Local Properties at Phase Transitions, Proceedings of the International School of Physics "Enrico Fermi," 1973, Varenna, Italy*, edited by K. A. Muller and A. Rigamonti (North–Holland, Amsterdam, 1976).

[29] A. D. Bruce and R. A. Cowley, J. Phys. C **6**, 2422 (1973).

[30] F. Z. He, B. O. Wells, Z. G. Ban, S. P. Alpay, S. Grenier, S. M. Shapiro, W. D. Si, A. Clark, and X. X. Xi, Phys. Rev. B **70**, 235405 (2004).

[31] F. Z. He, B. O. Wells, and S. M. Shapiro, Phys. Rev. Lett. **94**, 176101 (2005).

[32] P. A. Fleury and J. M. Worlock, Phys. Rev. **174**, 613 (1968).

[33] Y. L. Li, S. Y. Hu, Z. K. Liu, and L. Q. Chen, Appl. Phys. Lett. **78**, 3878 (2001).

[34] Y. L. Li, S. Y. Hu, Z. K. Liu, and L. Q. Chen, Acta Mater. **50**, 395 (2002).

[35] Y. L. Li, S. Y. Hu, Z. K. Liu, and L. Q. Chen, Appl. Phys. Lett. **81**, 427 (2002).

[36] A. Sharan, J. Lettieri, Y. F. Jia, W. Tian, X. Q. Pan, D. G. Schlom, and V. Gopalan, Phys. Rev. B **69**, 214109 (2004).

[37] V. Gopalan and R. Raj, J. Am. Ceram. Soc. **78**, 1825 (1995).

[38] V. Gopalan and R. Raj, J. Am. Ceram. Soc. **79**, 3289 (1996).

[39] V. Gopalan and R. Raj, J. Appl. Phys. **81**, 865 (1997).

[40] V. Gopalan and R. Raj, Appl. Phys. Lett. **68**, 1323 (1996).

[41] Y. Barad, J. Lettieri, C. D. Theis, D. G. Schlom, V. Gopalan, J. C. Jiang, and X. Q. Pan, J. Appl. Phys. **89**, 1387 (2001).

[42] Y. Barad and V. Gopalan, Integr. Ferroelectr. **44**, 19 (2002).

[43] A. Vasudevarao, A. Kumar, L. Tian, J. H. Haeni, Y. L. Li, D. G. Schlom, L. Q. Chen, Q. X. Jia, and Venkatraman Gopalan (unpublished, 2006).

[44] A. Antons, J. B. Neaton, K. M. Rabe, and D. Vanderbilt, Phys. Rev. B **71**, 024102 (2005).